Rare Met. (2022) 41(8):2894–2905
https://doi.org/10.1007/s12598-022-01986-3

RARE METALS

ORIGINAL ARTICLE

Heterostructuring an equiatomic CoNiFe medium-entropy alloy for enhanced yield strength and ductility synergy

Xin-Xin Ding, Jing Wang, Dong Liu, Chang Wang, Ping Jiang, Hua Qu, Guang-Hua Liu*, Fu-Ping Yuan, Xiao-Lei Wu*

Received: 7 November 2021 / Revised: 7 December 2021 / Accepted: 11 December 2021 / Published online: 22 May 2022

Abstract High-/medium-entropy alloys (H/MEAs) of face-centered-cubic-structured single phase usually suffer from a glaring drawback of low yield strength. Even worse, the trade-off emerges frustratingly between strength and ductility as strength increases. Here, the lamellar heterostructure (HS) is designed in an equiatomic ternary CoNiFe MEA by means of cold rolling followed by an incomplete recrystallization annealing. The lamellar HS consists of the soft recrystallized grains as well as severely deformed structures which are partly reserved. By comparison to the coarse-grained counterpart, the lamellar HS, shows a well enhanced yield strength-ductility synergy, together with an increased yield strength. This is ascribed to the hetero-deformation-induced (HDI) stress in HS during tensile deformation. Accordingly, the HDI strain hardening is induced, serving as an important addition to the conventional forest hardening. The HDI hardening is evidenced experimentally to account for a large proportion of global strain hardening. Furthermore, a fully recrystallized microstructure is obtained to show a simultaneous increase in both yield strength and ductility. The microstructures are evaluated in detail prior to and after tensile deformation by using the electron backscattered diffraction and transmission electron microscope observations. The mechanism for HDI strain hardening in various microstructures is analyzed to correlate to the evolution of microstructures in terms of the kernel average misorientation values, Schmid factor, and dislocation behaviors in response to plastic deformation.

Keywords Heterostructure (HS); Medium-entropy alloy (MEA); Hetero-deformation; Ductility; Strength

1 Introduction

High-/medium-entropy alloys (H/MEAs), since their advent [1, 2], have aroused great interest so far [3–6]. It is increasingly recognized that H/MEAs behave much like the conventional metals and alloys at least with regard to plastic deformation, along with the mechanism for strengthening and toughening [5–7], no matter whether face-centered cubic (fcc) or body-centered cubic (bcc)-structured. In this regard, even with an intrinsic hallmark toughness [5, 6, 8, 9], the typical fcc H/MEAs have inherited a few ineradicable problems from the conventional alloys and unfortunately, shown up in their macroscale mechanical properties. To be specific, two long-lasting issues appear in the relationship between strength and ductility, as two crucial properties for structural applications of H/MEAs. The first is the insurmountable trade-off between strength and ductility [5–7, 10–13] which are conflicting mutually. Namely, an increase in

X.-X. Ding, H. Qu, G.-H. Liu*
School of Physical Science and Technology, Tiangong University, Tianjin 300387, China
e-mail: liuguanghua@tiangong.edu.cn

X.-X. Ding, J. Wang, D. Liu, P. Jiang, F.-P. Yuan, X.-L. Wu*
State Key Laboratory of Nonlinear Mechanics, Institute of Mechanics, Chinese Academy of Science, Beijing 100190, China
e-mail: xlwu@imech.ac.cn

D. Liu, F.-P. Yuan, X.-L. Wu
School of Engineering Science, University of Chinese Academy of Sciences, Beijing 100049, China

C. Wang
Special Steel Department, Central Iron and Steel Research Institute, Beijing 100081, China

strength, by e.g., cold work and grain refinement, is at the expense of ductility [14]. The reason behind it is the lack of forest strain hardening based on dislocation plasticity [6, 7, 14]. Namely, the gradually diminishing hardening cannot catch up with the increase in flow stress during plastic deformation according to the Considère criterion [14]. The second is low yield strength at least for the vast majority of fcc H/MEAs of single phase [5–7, 10–13], which is also a glaring problem in conventional fcc counterparts [15]. In practice, ductility is always the crux of the problem. So far, almost all conventional microstructure-oriented mechanisms for strain hardening can be found in H/MEAs, including grain refinement [11], precipitation and second phase [10, 16–18], and annealing/deformation twins and specific dislocation pattern [13], along with the transformation-induced and twinning induced-plasticity effect [11, 19], etc.

Recently, the strategy by heterostructuring the traditional microstructure is proposed to enhance the strength-and-ductility synergy [20, 21]. By comparison to the homogeneous microstructure, the heterostructure (HS) features, to be simple, a combination of soft and hard grains, showing sharp contrasts in flow behaviors [20, 22]. These grains of plastic incompatibility will form hetero-boundaries where strain gradient appears locally due to the non-uniform deformation. To accommodate strain gradient, the geometrically necessary dislocations (GNDs) are produced [20, 23]. On the one hand, the GNDs will provide compatible deformation at hetero-boundaries; otherwise, plastic instability will occur there at first. On the other hand, GNDs, usually in their initial form of dislocation pile-ups [24, 25], further lead to the back stress in soft grains and forward stress in hard ones upon straining [20, 21], both of which are applied exactly at the hetero-boundary. The combination of back and forward stress is defined later as the hetero-deformation induced (HDI) stress [20, 21]. This HDI stress will facilitate an extra HDI strain hardening [20], serving as an effective supplement to the traditional forest hardening. Heterostructures of various kinds are thus designed and tailored for this synergistic effect of strain hardening, typical examples including gradient structure [26], lamellar structure [27], multi-level grain [12] and core–shell structure [28], etc.

The lamellar HS is a simple and easy-to-implement microstructural strategy for ductility [22, 27]. Cold work, e.g., cold rolling, will allow the original equiaxed grains to be deformed into the commonly fiber/lamella-like deformation structure, which later may be reserved partially during recrystallization annealing. This produces the lamellar HS, which is featured by the recrystallized equiaxed grains, along with the deformation structure of varying proportions in the form of dispersedly distributed lamellae. This lamellar HS shows the synergistic effect of reinforced strain hardenability for an enlarged ductility especially at high yield strength [27].

In the present study, the equiatomic ternary CoNiFe MEA of fcc-structured single phase was selected as a modal alloy [29–32]. Yield strength of this alloy seems to be the lowest [7] in the coarse-grained microstructure by comparison to other typical quinary (e.g., CrMnFeCoNi) and ternary alloys (e.g., CoNiCr, CoNiV) with a low stacking fault energy (SFE). This alloy has a medium SFE of 70 $mJ{\cdot}m^{-2}$ [33] and therefore, dislocation plasticity is dominant during tensile deformation. This makes CoNiFe MEA an appropriate candidate to motivate the HS strategy. More importantly, the lamellar-type deformation structure will be easily reserved to form HS, as compared to other H/MEAs of low SFE. In the following, we will show the lamellar HS in this CoNiFe MEA to realize a well enhanced strength-ductility synergy, together with an increased yield strength.

2 Experimental

CoNiFe MEA was produced by arc-melting pure cobalt, nickel, and iron (all > 99.9 wt% purity) under an argon atmosphere and cast into a 130 mm diameter iron mold. The ingot was re-melted three times to ensure chemical homogeneity, with the composition of 32.1 at% Co, 32.1 at% Ni, and 35.8 at% Fe. The ingot was then hot-forged and hot-rolled at 1150 °C to a thick plate of 12 mm × 70 mm × 800 mm in dimension, followed by homogenization treatment at 1150 °C for 24 h in vacuum and final quenching in water. This thick plate was cold-rolled to a 1.0-mm-thick thin sheet at thickness reduction of 90%. Finally, HSs of two kinds, here named as HS_1 and HS_2, respectively, were obtained by partial recrystallization annealing at 620 °C for 10 and 5 min. The fine-grained (labeled as FG) and coarse-grained (CG) microstructure were obtained after annealing at 700 °C for 4 min and 1000 °C for 30 min, respectively.

Tensile specimens of gauge cross-section of 4 mm × 1 mm × 15 mm were cut from thin sheets, with the longitudinal axis parallel to rolling direction. The uniaxial tensile tests were performed at room temperature and strain rate of 5×10^{-4} s^{-1} in an MTS 793 machine. An extensometer was used for tensile strain measurements.

The unload-reload tensile deformation was conducted to test HDI stress (σ_{HDI}). Upon straining to a designated strain, the specimen was unloaded by the stress-control mode to 50 N, followed by reloading to the same applied stress before next unloading. σ_{HDI} is determined as [34]:

$$\sigma_{HDI} = \frac{\sigma_r + \sigma_u}{2} \quad (1)$$

where σ_u and σ_r are yield stress upon unloading and reloading determined from the hysteresis loop, respectively.

The microstructure was characterized by using X-ray diffraction (XRD) analysis, electron backscattered diffraction (EBSD), and transmission electron microscope (TEM) observations. XRD was conducted using XRD with Cu target operating at 9 kW (Rigaku Smart Lab X-ray diffractometer with the Cu Kα radiation at 45 kV and 200 mA). The samples were scanned through the 2θ range from 20° to 100° with a step size of 0.01° and a counting time of 1 s. EBSD imaging was conducted in a ZEISS Gemini 300 SEM with an EBSD detector. The samples for EBSD observations were mechanically polished, followed by electro-polishing in a solution of 5% perchloric and 95% alcohol at 30 V. TEM observations were performed in a Tecnai $G^2$20 operated at 200 kV. All TEM films were mechanically polished to 50 μm in thickness and punched to the discs of 3 mm in diameter. Perforation was carried out by twin-jet electro-polishing at 25 °C and 30 mA in a solution of 5 vol% perchloric acid and 95 vol% alcohol. TEM foils for microstructural observations after tensile testing were cut from the gauge section.

3 Results and discussion

3.1 Microstructural characterization

3.1.1 CG microstructure

Figure 1 characterizes the microstructure in the as-annealed CG of CoNiFe MEA. Figure 1a indicates that the microstructure keeps the single fcc phase in CG and all other microstructures before and after tensile deformation. Figure 1b, c is, respectively, EBSD inverse pole figure (IPF) and grain boundary (GB) figure. An average size of 90.1 μm is shown in the statistic distribution of grain size in CG (upper panel, Fig. 1d). Interestingly, this CoNiFe of medium SFE has annealing twins of high density, with the proportion of twin boundary (TB) of as high as 50% (lower panel, Fig. 1d).

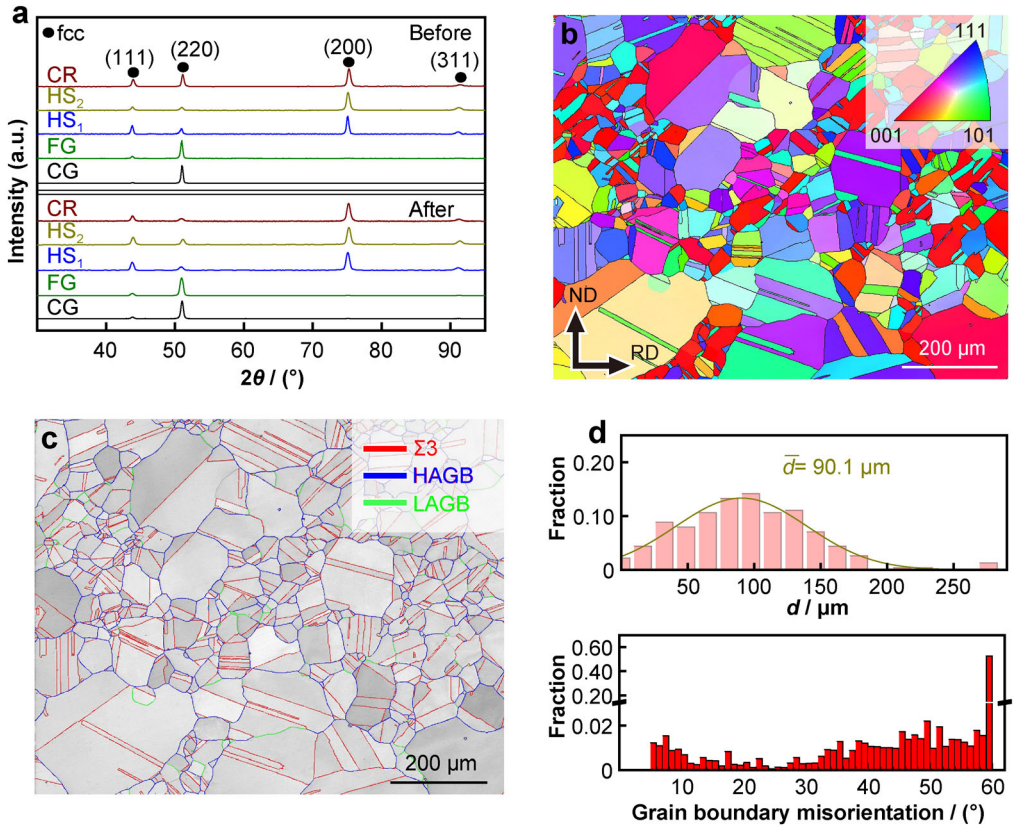

Fig. 1 Microstructure of as-annealed CG in CoNiFe MEA: **a** XRD patterns of various microstructures before and after tensile deformation, where HS is heterostructures (subscript: varying recrystallization annealing) and CR, FG, and CG are cold-rolled, fine-grained, and coarse-grained structure, respectively; **b** EBSD IPF; **c** GB figure, where Σ3 is twin boundary (TB), HAGB/LAGB is high-angle/low-angle grain boundary; **d** distribution of both grain size (upper panel) and grain boundary misorientation (lower panel)

3.1.2 HS microstructure

Figure 2 shows the microstructure in HS_1. The thin lamellae of deformed structure (DS) are visible after incomplete recrystallization (Fig. 2a), along with the recrystallized equiaxed grains, labeled as RGs. The lamellae are featured by the low-angle grain boundaries (LAGB) (Fig. 2b). Interestingly, annealing twins of high density appear in the interiors of RGs. As the grain reference orientation deviation (GROD) figure in Fig. 2c indicated, the smaller the GROD values are, the larger the degree in grains where recrystallization annealing completes will be. Except for RGs with small GROD values in blue, all other areas show larger GROD values. As such, the DS in HS_1 is in a deformation state of varying degrees. The microstructure in HS_1 is further detailed in terms of the kernel average misorientation (KAM) figure. The KAM values are larger in lamellae (mainly in green, Fig. 2d) than those in recrystallized grains (in blue), indicating the presence of more GNDs at lamella boundaries for compatible deformation. As the Schmid factor figure present (Fig. 2e), there are a large range variations of Schmid factors in both RGs and DS. Figure 2f is a close-up view only for RGs, by getting rid of DS (areas in black). Figure 2g is also the close-up view of EBSD quality figure overlaid with GB figure, clearly showing RGs with annealing twins inside. The bright-field TEM image in Fig. 2h shows that the RGs have annealing twins and stacking faults inside, almost free of dislocations. As shown in the statistic distribution of both the grain size (upper panel) and grain boundary misorientation (lower panel) for RGs (Fig. 2i), the average grain size is 7.1 μm in HS_1, along with a large proportion of 66% for annealing twins. The proportion of deformed lamellae in HS_1 is averaged to be 40% according to the statistical analyses based on both KAM and GROD figures.

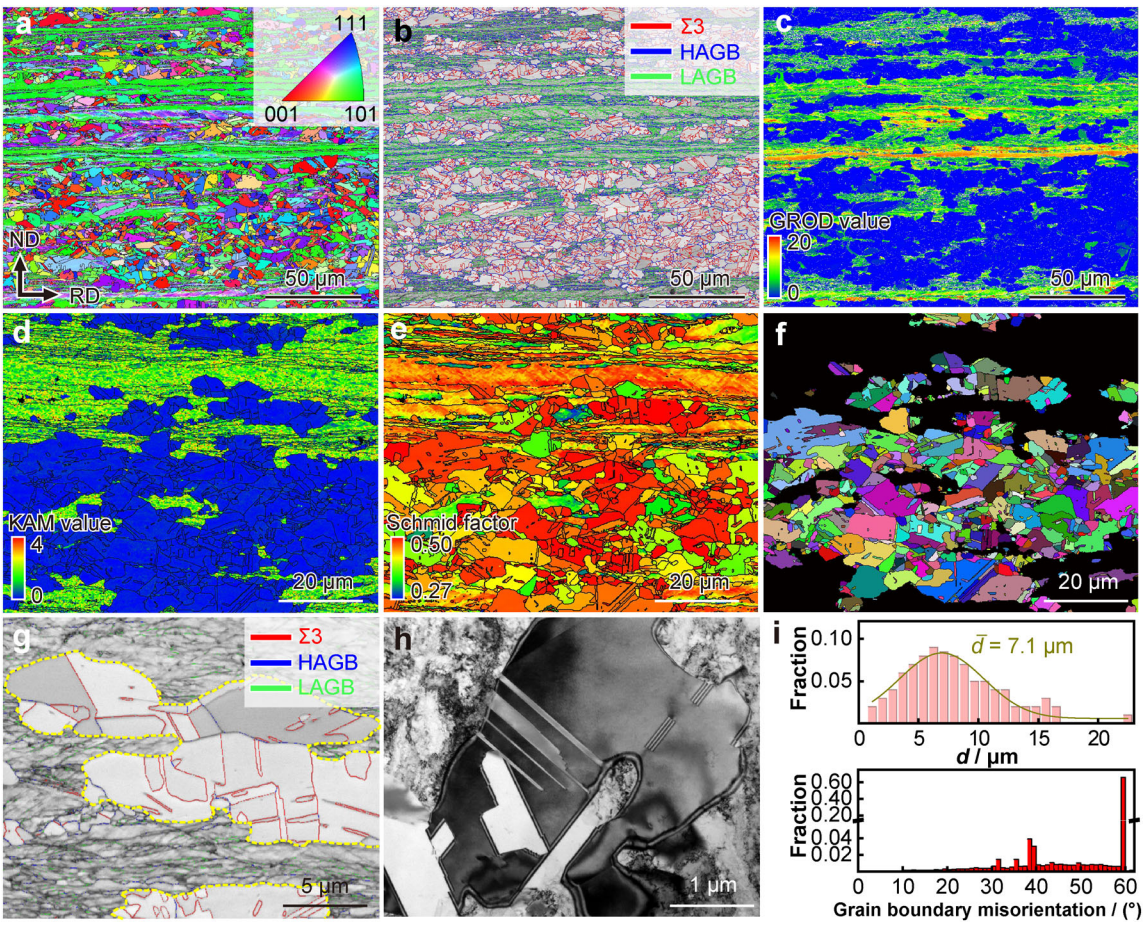

Fig. 2 Microstructure of HS_1: **a** EBSD IPF, where deformed structures of elongated lamellae are reserved, along with recrystallized equiaxed grains, and RD/ND is rolling and normal direction during cold rolling; **b** EBSD GB figure, where lamellae are circled by LAGBs (in green); **c** GROD figure; **d** KAM figure; **e** Schmid factor figure; **f** recrystallized grains; **g** close-up view of EBSD quality figure overlaid GB figure, where red lines are TBs; **h** TEM bright-field image of recrystallized grain; **i** distribution of grain size (upper panel) and grain boundary misorientation (lower panel) in recrystallized grains

Another HS, labeled as HS_2, is further designed (Fig. 3) to maintain more DS for even higher strength than those in HS_1. EBSD IPF in Fig. 3a overlays the Schmid factor image of well-recognized RGs. The microstructure exhibits two typical features. One is the lamellae of DS with more proportion than that in HS_1, while the other is equiaxed RGs dispersedly distributed. GROD (upper panel) and KAM value (lower panel) figures (Fig. 3b) both indicate less RGs (colored in blue) than those in HS_1. EBSD GB image (upper panel) and its close-up view (lower panel) (Fig. 3c) show similar feature of RGs to that in HS_1. As the statistic distribution of both grain size (upper panel) and grain boundary misorientation (lower panel) shown, the average grain size of RGs decreases to 3.1 μm in HS_2, along with the proportion of around 15% (Fig. 3d).

3.1.3 Fine-grained (FG) microstructure

FG microstructure is completely recrystallized, as seen in EBSD IPF (Fig. 4a) and GB image (Fig. 4b), with no sign of reserved DS, as evidenced by GROD (upper panel, Fig. 4c) and KAM value figures (lower panel, Fig. 4c). The average grain size of FGs is 8.1 μm, which is much smaller than that of CG.

3.2 Tensile mechanical property

3.2.1 Strength-and-ductility synergy

Figure 5a is a set of tensile engineering stress–strain ($\sigma_e-\varepsilon_e$) curves in various microstructures. Thereinto, the deformation structure after cold rolling (CR) shows the ceiling-floor yield strength (σ_y) as high as 960 MPa. Necking happens soon after yielding, with hardly any uniform tensile elongation (ε_u), i.e., ductility. The CG after full recrystallization shows the lowest σ_y of as low as 160 MPa, together with ε_u of 27%. Now, we place the emphasis on other three $\sigma_e-\varepsilon_e$ curves with σ_y in between. The first is HS_1. σ_y rises to 630 MPa, which is about four times that in CG, even lower than that after CR. HS_1 shows an acceptable ε_u of 12%. The second is HS_2. σ_y increases further by 200 to 830 MPa by comparison to HS_1, still

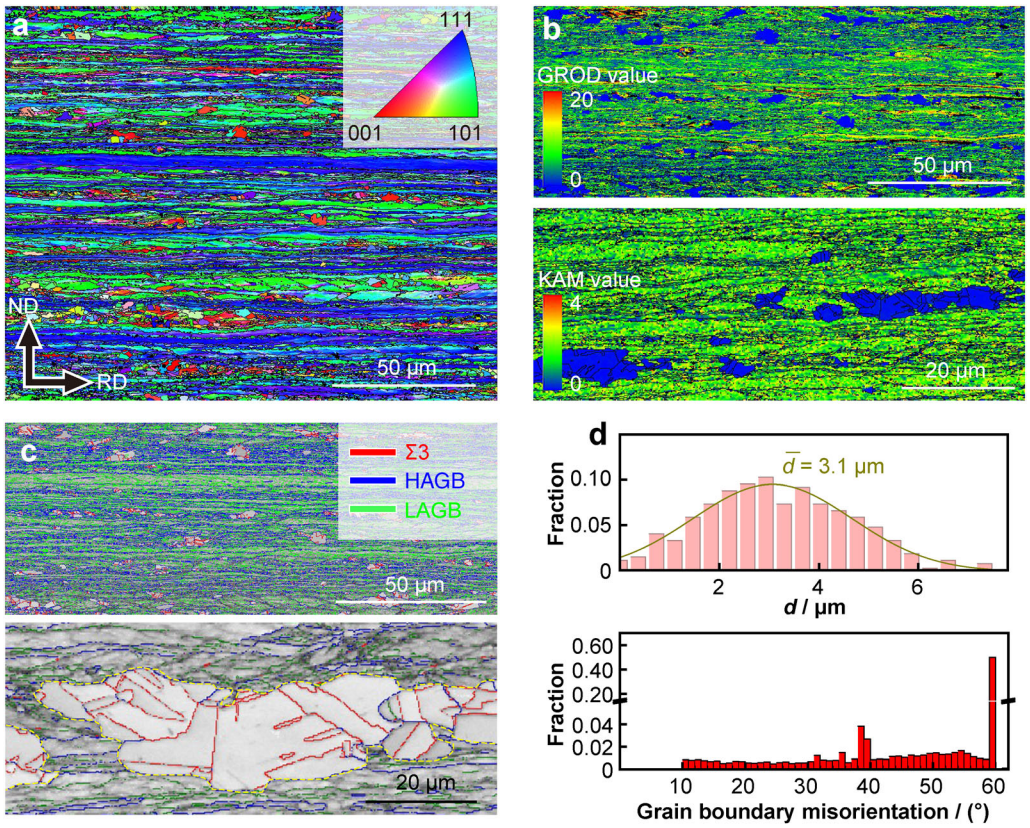

Fig. 3 Microstructure of HS_2: **a** EBSD IPF overlaid with Schmid factor figure; **b** GROD (upper panel) and KAM figure (lower panel); **c** EBSD GB figure (upper panel) and close-up view (lower panel), where dash line in yellow is RG; **d** distribution of grain size (upper panel) and grain boundary misorientation (lower panel)

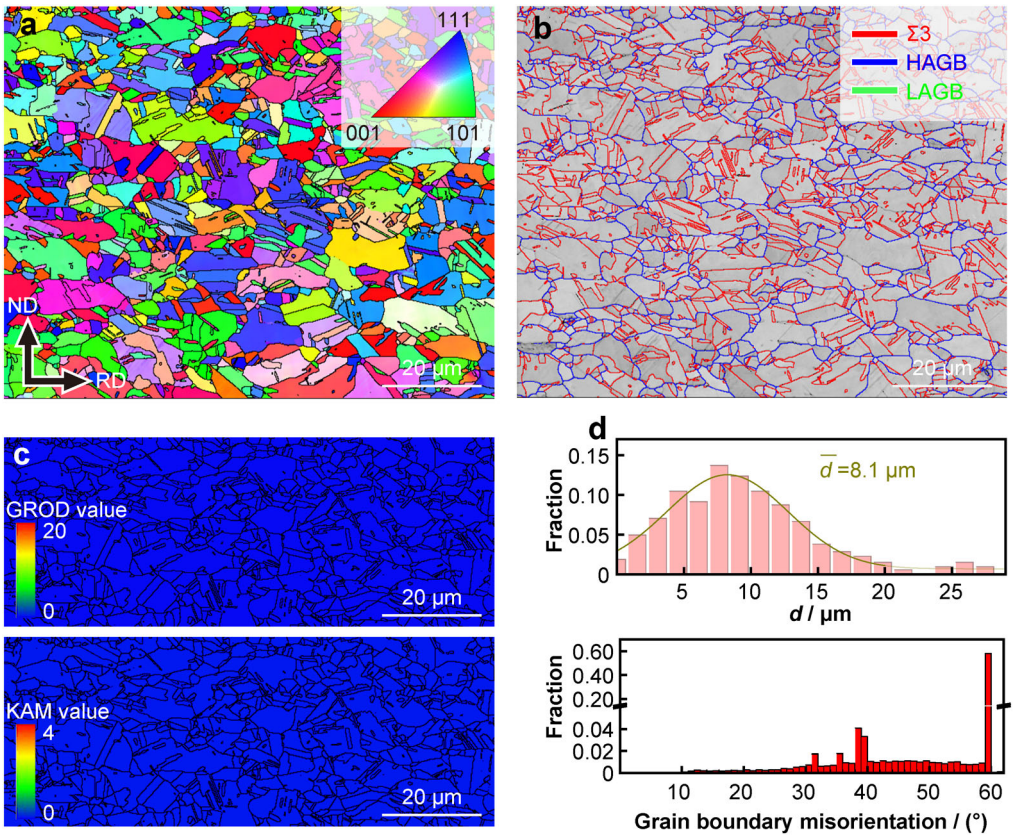

Fig. 4 Microstructure of FG: **a** EBSD IPF; **b** EBSD GB figure; **c** GROD (upper panel) and KAM value figure (lower panel); **d** distribution of grain size (upper panel) and grain boundary misorientation (lower panel)

keeping ε_u of 5%. Accordingly, the (σ_y, ε_u) trade-off still holds for two HS microstructures. Namely, the HS strategy is able to relieve effectively the (σ_y, ε_u) trade-off, instead of evading it. Last but not least, of interest note is FG structure. σ_y doubles as compared to that of the CG counterpart, along with the simultaneous increase in σ_y and ε_u, as seen from the $\sigma_e-\varepsilon_e$ curve. Figure 5b is the corresponding true stress–true strain ($\sigma_T-\varepsilon_T$) curves. Figure 5c shows the strain hardening rate ($\theta = \frac{\partial\sigma}{\partial\varepsilon}$) normalized by σ_T ($\theta = \frac{\partial\sigma}{\partial\varepsilon}\cdot\frac{1}{\sigma_T}$) curves, all as a function of ε_T. It is visible that θ of CR plunges to necking, while θ of CG shows the most sluggish decrease. Interestingly, θ in HS_1 and HS_2 shows the downtrend almost similar to that of CG as ε_T increases. Particularly, θ in FG is even higher than that for CG. Note an enhanced σ_y in HS_1, HS_2, and FG, it follows that there is the unique strain hardening to take effect in these microstructures. Figure 5d shows the (σ_y, ε_u) combination. For comparison, a few other data (dash line) is also shown from homogeneous microstructures in the CoNiFe MEA [29–32]. An obvious rise of (σ_y, ε_u) combination is visible to the top right. Importantly, ε_u in the present HS and FG is larger than those at similar levels of σ_y of homogeneous microstructures.

3.2.2 HDI stress and HDI hardening

The HDI strain hardening is evaluated by load-unload-reload (LUR) tensile testing. Figure 6a shows the $\sigma_T-\varepsilon_T$ curves with a series of interrupted unload strains for the microstructures of four kinds. Figure 6b is close-up views, respectively, at small ($\sim$ 1%, upper panel) and large unload strain ($\sim$ 10%, lower panel). It is visible that the mechanical hysteresis loop appears already at strain of 1% in HS_1, HS_2, and FG, except for the CG. These hysteresis loops signal the onset of reverse plastic flow upon unloading even though the applied stress is still in tension [21, 22]. This is an unambiguous sign that the HDI stress (σ_{HDI}) is formed to take effect [12, 22]. The loop width, defined as the residual plastic strain (ε_{rp}), is used to characterize the HDI effect [12]. Interestingly, ε_{rp} in HS_1 is large initially and then decrease gradually (Fig. 6c). By contrast, ε_{rp} in CG gradually increases and then levels off. Yet, it is worthy to note the higher ε_{rp} in HS_1 than in CG. ε_{rp} in the other two is larger than that in CG at first, but keeps almost constant later. Importantly, as shown in Fig. 6d, σ_{HDI} is the largest in HS_2, while it is the smallest in CG, showing the uptrend as σ_y increases. Figure 6e, f

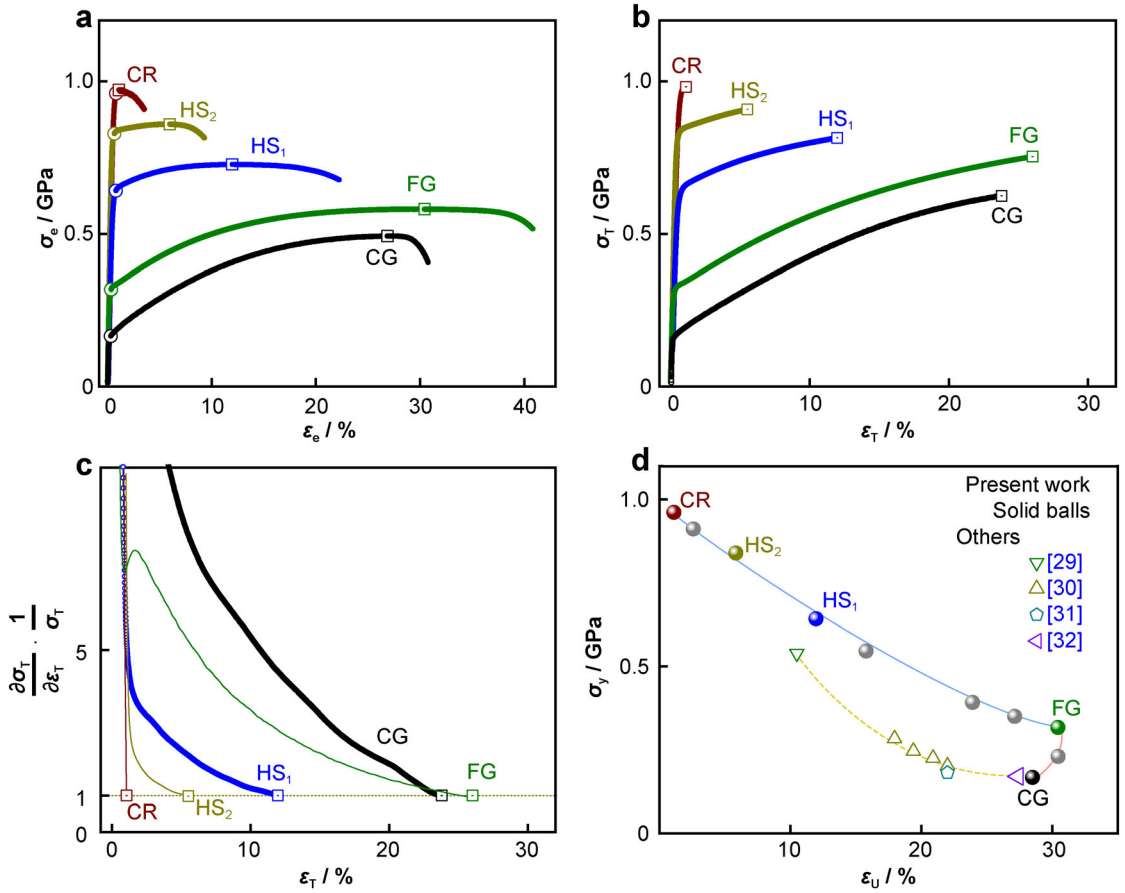

Fig. 5 Tensile properties of CoNiFe MEA in various microstructures: **a** σ_e–ε_e curves, where circle is yield strength (σ_y), square is ultimate tensile strength (UTS) corresponding to uniform tensile elongation (ε_u), CR and CG are coarse grained and cold-rolled microstructure, and HS_1/HS_2 and FG are heterostructure and fine-grained after incomplete and full recrystallization annealing, respectively; **b** σ_T–ε_T curves; **c** normalized θ–ε_T curves; **d** (σ_y, ε_u) balance, where other data for homogeneous microstructures in CoNiFe are shown for comparison

shows the proportion of σ_{HDI} to σ_{flow} and that of strain hardening rate by σ_{HDI} (θ_{HDI}) to θ_{flow}, respectively. It is visible that both $\sigma_{HDI}/\sigma_{flow}$ and $\theta_{HDI}/\theta_{flow}$ in HS_1 and HS_2 are larger than those of CG and FG during the initial stage of tensile deformation. FG even show a larger $\theta_{HDI}/\theta_{flow}$ than CG with tensile deformation.

3.3 Microstructural evolution during tensile deformation

Both KAM value and Schmid factor are measured before and after tensile deformation in CG, HS_1 and FG, respectively, to describe the microstructural evolution in response to plastic deformation. Figure 7 summarizes the results and Fig. 8 is the corresponding statistical analysis.

Figure 8a shows the KAM values near the grain boundary and twin boundary in CG before and after tensile deformation. The average KAM value ($\overline{K}$) increases from 0.15 to 0.55, along with an enhanced proportion of large KAM values. This indicates the plastic hetero-deformation to occur even in CG, leading to the production of GNDs. This is exactly the reason for hysteresis loops to appear in CG (Fig. 6b). For HS_1, $\overline{K}$ increases in RG (middle panel, Fig. 8a), with an obvious decrease in DS. FG shows the trend in KAM value (lower panel, Fig. 8a) similar to that of CG. Figure 8b compares the Schmid factor distribution in these three microstructures before and after tensile deformation. For CG (upper panel, Fig. 8b), RG in HS_1 (middle panel), and FG (lower panel), the average Schmid factor value ($\overline{F}$) decreases after deformation, along with an increased proportion for small values of Schmid factor. Of special note is DS in HS_1 (middle panel), showing an obviously decrease in $\overline{F}$, along with an increase in the proportion of low values. This indicates that the reserved deformation structures also experience plastic deformation.

Figure 9 is a set of TEM micrographs mainly showing the varying dislocation sub-structures after tensile deformation in HS_1, HS_2, and FG, respectively. Figure 9a shows

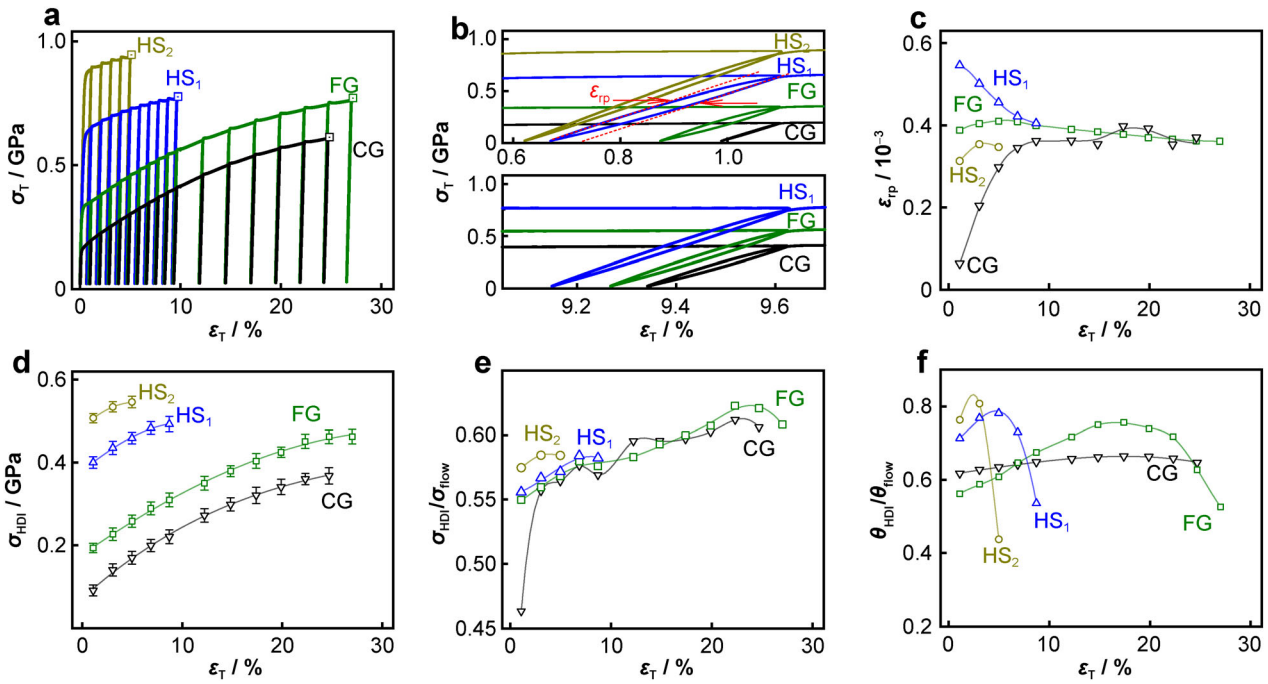

Fig. 6 HDI stress and hardening by LUR tensile tests. **a** $\sigma_T-\varepsilon_T$ curves in four microstructures; **b** mechanical hysteresis loops at unload strain of ~ 1% (upper panel) and ~ 10% (lower panel); **c** ε_{rp}–ε_T curves; **d** $\sigma_{HDI}-\varepsilon_T$ curves; **e** $\sigma_{HDI}/\sigma_{flow}$–$\varepsilon_T$ curves; **f** $\theta_{HDI}/\theta_{flow}$–$\varepsilon_T$ curves

one RG as well as ambient DS in HS_1. Figure 9b, c is two close-up views of DS and RG, respectively. The dislocations with high density mutually entangle in DS (Fig. 9b). Similarly, the dislocations in RGs distribute non-homogeneously. Interestingly, both HS_1 and HS_2 show a common feature that the dislocation density is higher near the GBs and TBs than inside the interiors (Fig. 9d–f). Meanwhile, the density of dislocations inside the grain interiors is lower in HS_2 (Fig. 9e) than in HS_1 (Fig. 9d). In FG, the dominant dislocation behavior is the formation of dislocation tangles and cells (Fig. 9g). The close-up view shows the pile-up of dislocations ahead of the cell boundary, as shown in Fig. 9h.

3.4 Discussion

The present HS_1 and HS_2 exhibit an enhanced strength-and-ductility synergy compared to their CG counterpart (Fig. 5a, d). Here, the GBs in RGs, along with TBs of high density, serve as hetero-interfaces where GNDs are produced during plastic deformation. This is reflected by an obvious increment in KAM values (middle panel, Fig. 8a). These GNDs act as the origin of both HDI stress and corresponding HDI strain hardening as well [20, 21]. Importantly, both HDI stress and extra HDI strain hardening account for a large proportion of flow stress and global hardening in HS_1 (Fig. 6e, f). This is the extraordinary synergistic effect in HS for strain hardening, which is the reason that the trade-off in strength and ductility can be largely alleviated in HS.

The important role of hetero-interfaces in HS_1, including GBs and TBs, is elucidated to facilitate HDI strain hardening in terms of the change in KAM values. $\overline{K}$ increases from 0.15 (before tensile deformation) to 0.36 (after) in RG (middle panel, Fig. 8a), along with the simultaneous increase in the proportion of large KAM values. This indicates a crucial role by these boundaries to produce the GNDs for HDI hardening during tensile deformation. The TBs are considered to play the same role as GBs in blocking the gliding dislocations to form dislocation pile-ups exactly near TBs. More importantly, there is an obvious decrease in $\overline{K}$ for DS in HS_1 from 1.33 to 1.10 before and after tensile deformation (middle panel, Fig. 8a), indicating plastic accommodation that happens in DS. This is the result of forward stress, i.e., a component of HDI stress, which is exerted on the DS. The forward stress induces the activation of slip systems different from original ones [22], which facilitates the dislocation slip in the opposite direction and dis-entanglements of dislocations particularly at GBs [26]. This argument is consistent with the decrease in $\overline{F}$ for DS in HS_1 (middle panel, Fig. 8b). Moreover, the entangled dislocations of high density near GBs (Fig. 9d, e) and TBs (Fig. 9f) provide further evidences of HDI hardening which prefers to take effect at the hetero-interfaces.

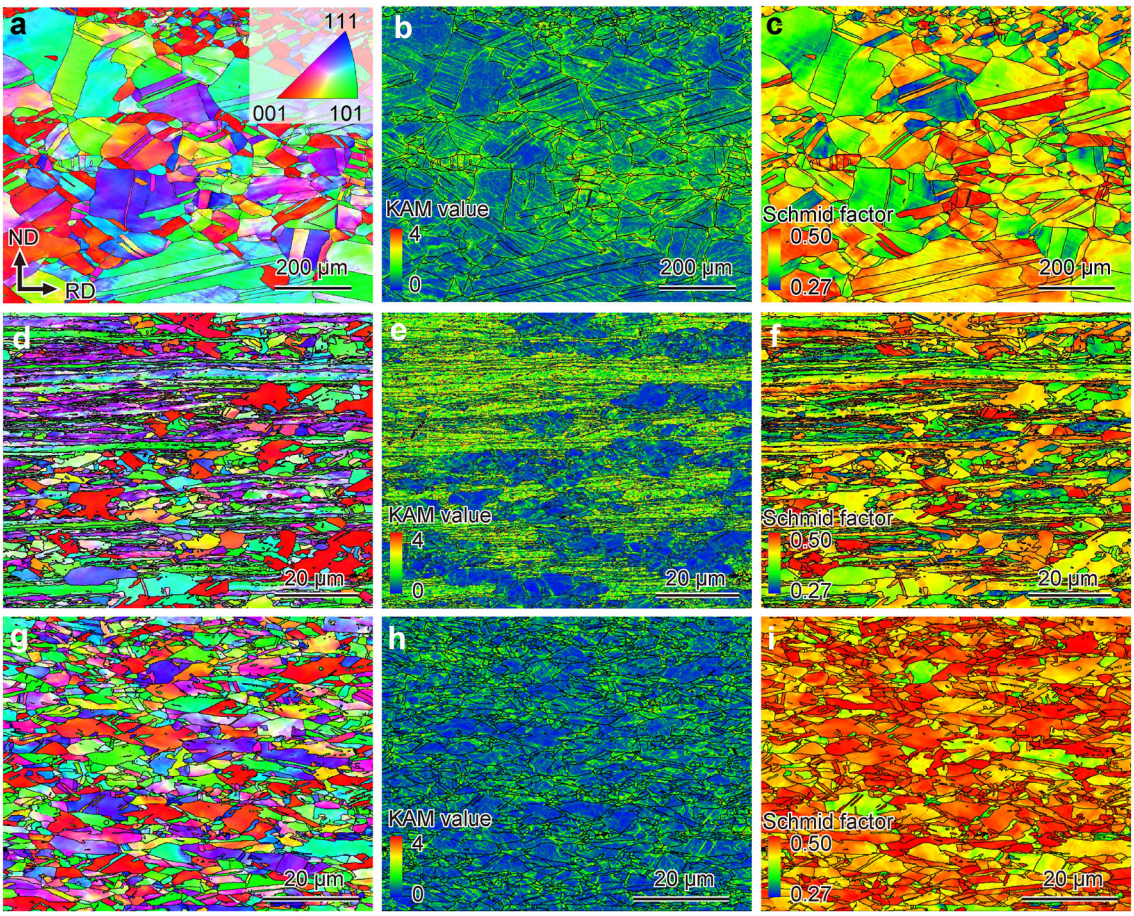

Fig. 7 EBSD microstructures in CG, HS_1 and FG after tensile deformation: **a–c** EBSD IPF, KAM value, and Schmid factor figure, respectively, in CG; corresponding results for **d–f** HS_1 and **g–i** FG

FG exhibits the impressive synergy between strength and ductility. FG shows the similar change in terms of both KAM value and Schmid factor (two lower panels), respectively, in Fig. 8a, b, by comparison to those for CG (two upper panels). Owing to the increase in the average grain sizes of RGs ($\overline{d}$ of 8.1 μm, Fig. 4d) compared to that in HS_1 ($\overline{d}$ of 7.1 μm, Fig. 2i), the dislocation behavior shifts from the entangled dislocations in HS_1 (Fig. 9c, d) to cells (Fig. 9g, h) in FG. Particularly, the dislocation pile-up (indicated by an arrow) is seen ahead of the sub-boundary of dislocation cell in FG, as seen in Fig. 9h. The pile-up is proposed to be the dislocation origin of HDI stress [20]. This is the reason that the mechanical hysteresis loop also occurs in FG (Fig. 6b). Both $\sigma_{HDI}/\sigma_{flow}$ and $\theta_{HDI}/\theta_{flow}$ show the similar trend in both FG and CG, as shown in upper and lower panels in Fig. 6e, f. Both are larger in FG than in CG during the later stage of tensile deformation. This is due to the size effect of dislocation pile-up for HDI stress.

4 Conclusion

By means of cold rolling followed by recrystallization annealing in an equiatomic ternary CoNiFe medium-entropy alloy, the lamellar HS was architecture to induce the extra strain hardening for ductility at elevated yield strength. The lamellar HS consists of ductile recrystallized grains as the base, along with the strong deformation structure which are reserved. HS of two kinds shows improved yield strength compared to the coarse-grained counterpart. Ductility is acceptable, even with deformation structures of hardly any ductility, which leads to an alleviated trade-off between yield strength and ductility. Particularly in a grain-refined microstructure, a simultaneous increase in both strength and ductility is achievable. The HDI plasticity is tested in varying microstructures to show HDI stress and HDI hardening, both of which account for a large proportion of global flow stress and strain hardening. The evolutions of deformation microstructures are characterized in detail. The change of kernel average

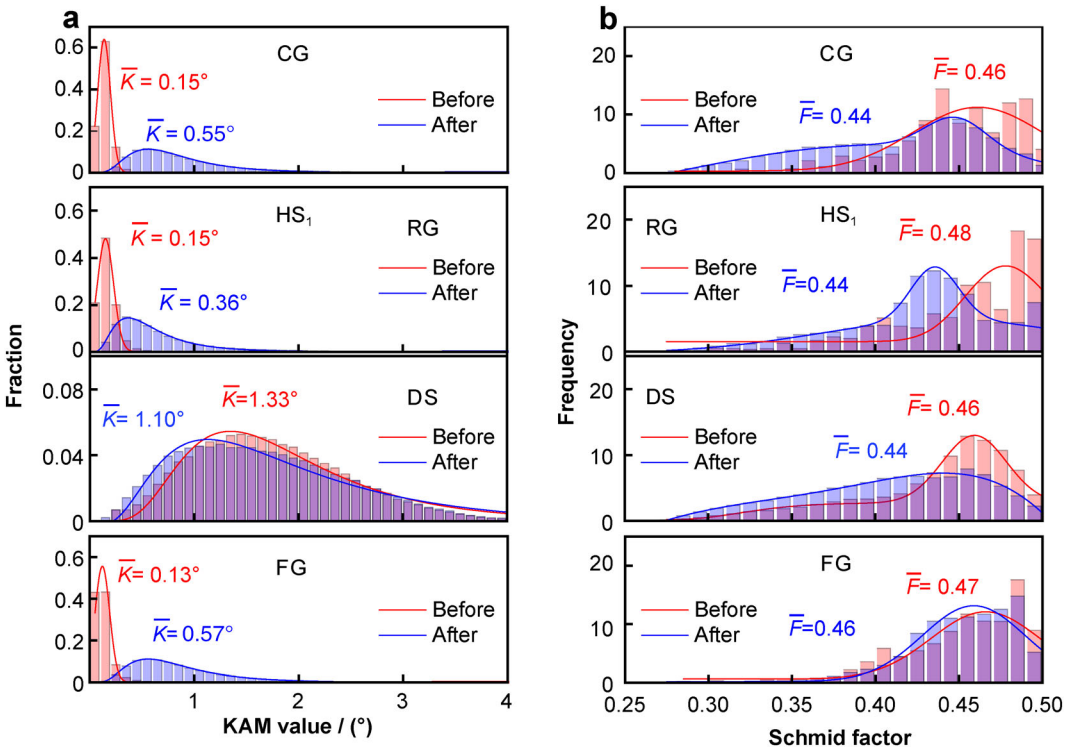

Fig. 8 Distribution of both KAM value and Schmid factor: **a** KAM value in CG (upper panel), HS_1 (middle two panels), and FG (lower panel) before and after tensile deformation; **b** corresponding Schmid factor analysis, where RG and DS are recrystallized grains and reserved deformation structure in HS_1, respectively

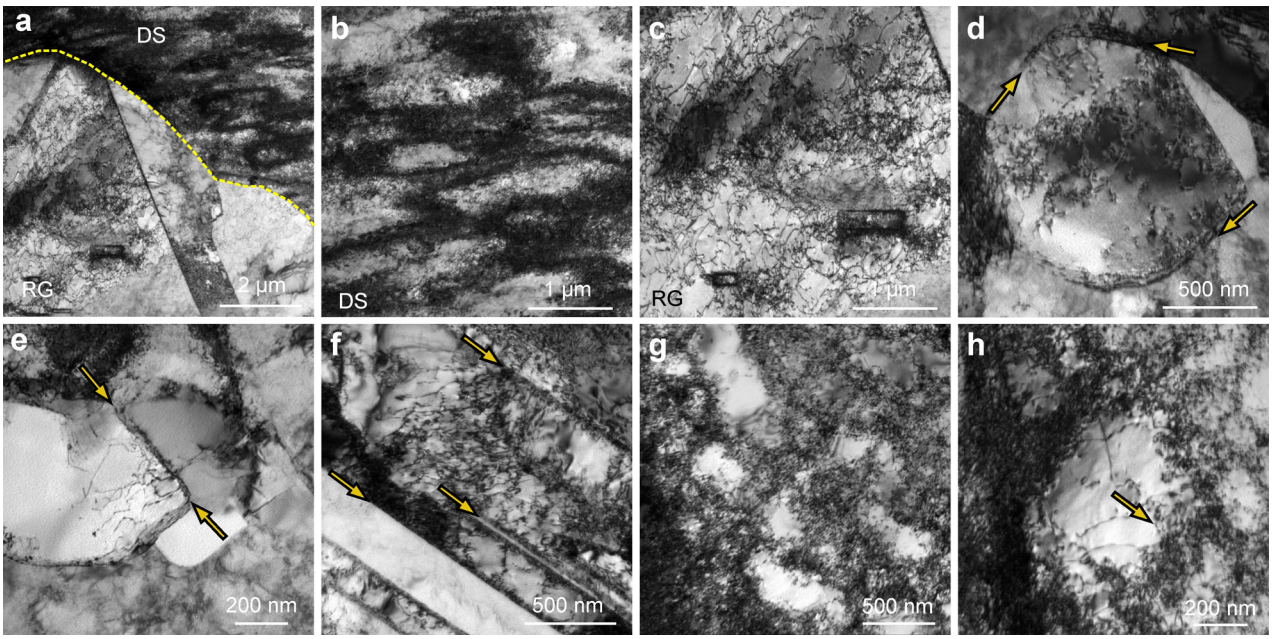

Fig. 9 TEM images showing dislocation behaviors after tensile deformation in HS_1, HS_2 and FG: **a** RG and neighboring DS in HS_1, where dash line are GB circles RG; **b**, **c** close-up views of DS and RG, respectively; entangled dislocations (arrows) near **d, e** GB respectively in HS_1 and HS_2 and **f** TB in HS_1; **g** dislocation cells inside FG; **h** close-up view showing dislocation pile-up ahead of cell boundary as pointed by an arrow

misorientation values, along with the direct observations of dislocation behavior, exhibits the production of geometrically necessary dislocations in the recrystallized grains as the origin of both HDI stress and HDI hardening.

Acknowledgements This study was financially supported by the National Key R&D Program of China (Nos. 2017YFA0204402 and 2019YFA0209900), the National Natural Science Foundation of China (Nos. 11972350 and 11790293) and the Strategic Priority Research Program of the Chinese Academy of Sciences (No. XDB22040503).

Declarations

Conflict of interests The authors declare that they have no conflict of interest.

References

[1] Yeh JW, Chen SK, Lin SJ, Gan JY, Chin TS, Shun TT, Tsau CH, Chang SY. Nanostructured high-entropy alloys with multiple principal elements: novel alloy design concepts and outcomes. Adv Eng Mater. 2004;6(5):299.
[2] Cantor B, Chang ITH, Knight P, Vincent AJB. Microstructural development in equiatomic multicomponent alloys. Mater Sci Eng, A. 2004;375:213.
[3] Li WD, Xie D, Li DY, Zhang Y, Gao YY, Liaw PK. Mechanical behavior of high-entropy alloys. Prog Mater Sci. 2021;118:100777.
[4] Wu Y, Zhang F, Yuan XY, Huang HL, Wen XC, Wang YH, Zhang MY, Wu HH, Liu XJ, Wang H, Jiang SH, Lu ZP. Short-range ordering and its effects on mechanical properties of high-entropy alloys. J Mater Sci Technol. 2021;62:214.
[5] George EP, Raabe D, Ritchie RO. High-entropy alloys. Nat Rev Mater. 2019;4(8):515.
[6] George EP, Curtin WA, Tasan CC. High entropy alloys: a focused review of mechanical properties and deformation mechanisms. Acta Mater. 2020;188:435.
[7] Ma E, Wu XL. Tailoring heterogeneities in high-entropy alloys to promote strength–ductility synergy. Nat Commun. 2019;10(1):5623.
[8] Yang HX, Li JS, Guo T, Wang WY, Kou HC, Wang J. Evolution of microstructure and hardness in a dual-phase $Al_{0.5}$CoCrFeNi high-entropy alloy with different grain sizes. Rare Met. 2020;39(2):156.
[9] Lu SY, Miao JW, Lu YP. Strengthening and toughening of multi-principal high-entropy alloys. Chin J Rare Met. 2021;45(5):530.
[10] Lei ZF, Liu XJ, Wu Y, Wang H, Jiang SH, Wang SD, Hui XD, Wu YD, Gault B, Kontis P, Raabe D, Gu L, Zhang QH, Chen HW, Wang HT, Liu JB, An K, Zeng QS, Nieh TG, Lu ZP. Enhanced strength and ductility in a high-entropy alloy via ordered oxygen complexes. Nature. 2018;563(7732):546.
[11] Li ZM, Pradeep KG, Deng Y, Raabe D, Tasan CC. Metastable high-entropy dual-phase alloys overcome the strength–ductility trade-off. Nature. 2016;534(7606):227.
[12] Yang MX, Yan DS, Yuan FP, Jiang P, Ma E, Wu XL. Dynamically reinforced heterogeneous grain structure prolongs ductility in a medium-entropy alloy with gigapascal yield strength. Proc Natl Acad Sci USA. 2018;115(28):7224.
[13] Pan QS, Zhang LX, Feng R, Lu QH, An K, Chuang AC, Poplawsky JD, Liaw PK, Lu L. Gradient-cell–structured high-entropy alloy with exceptional strength and ductility. Science. 2021;374(6570):984.
[14] Zhu YT, Wu XL. Ductility and plasticity of nanostructured metals: differences and issues. Mater Today Nano. 2018;2:15.
[15] Lu K. Stabilizing nanostructures in metals using grain and twin boundary architectures. Nat Rev Mater. 2016;1(5):16019.
[16] Yang T, Zhao YL, Tong Y, Jiao ZB, Wei J, Cai JX, Han XD, Chen D, Hu A, Kai JJ, Lu K, Liu Y, Liu CT. Multicomponent intermetallic nanoparticles and superb mechanical behaviors of complex alloys. Science. 2018;362(6417):933.
[17] He JY, Wang H, Huang HL, Xu XD, Chen MW, Wu Y, Liu XJ, Nieh TG, An K, Lu ZP. A precipitation-hardened high-entropy alloy with outstanding tensile properties. Acta Mater. 2016;102:187.
[18] Jiang SH, Xu XQ, Li W, Peng B, Wu Y, Liu XJ, Wang H, Wang XZ, Lu ZP. Strain hardening mediated by coherent nanoprecipitates in ultrahigh-strength steels. Acta Mater. 2021;213:116984.
[19] Li ZM, Tasan CC, Pradeep KG, Raabe D. A TRIP-assisted dual-phase high-entropy alloy: grain size and phase fraction effects on deformation behavior. Acta Mater. 2017;131:323.
[20] Zhu YT, Wu XL. Perspective on hetero-deformation induced (HDI) hardening and back stress. Mater Res Lett. 2019;7(10):393.
[21] Zhu YT, Ameyama K, Anderson PM, Beyerlein IJ, Gao HJ, Kim HS, Lavernia E, Mathaudhu S, Mughrabi H, Ritchie RO, Tsuji N, Zhang XY, Wu XL. Heterostructured materials: superior properties from hetero-zone interaction. Mater Res Lett. 2020;9(1):1.
[22] Wu XL, Zhu YT, Lu K. Ductility and strain hardening in gradient and lamellar structured materials. Scr Mater. 2020;186:321.
[23] Gao HJ, Huang YG. Geometrically necessary dislocation and size-dependent plasticity. Scr Mater. 2003;48(2):113.
[24] Mughrabi H. On the role of strain gradients and long-range internal stresses in the composite model of crystal plasticity. Mater Sci Eng, A. 2001;317(1):171.
[25] Han CS, Gao HJ, Huang YG, Nix WD. Mechanism-based strain gradient crystal plasticity—II. Analysis J Mech Phys Solids. 2005;53(5):1204.
[26] Wu XL, Jiang P, Chen L, Yuan FP, Zhu YT. Extraordinary strain hardening by gradient structure. Proc Natl Acad Sci U S A. 2014;111(20):7197.
[27] Wu XL, Yang MX, Yuan FP, Wu GL, Wei YJ, Huang XX, Zhu YT. Heterogeneous lamella structure unites ultrafine-grain strength with coarse-grain ductility. Proc Natl Acad Sci U S A. 2015;112(47):14501.
[28] Sekiguchi T, Ono K, Fujiwara H, Ameyama K. New microstructure design for commercially pure titanium with outstanding mechanical properties by mechanical milling and hot roll sintering. Mater Trans. 2010;51(1):39.
[29] Guo YH, Li MY, Li P, Chen CG, Zhan Q, Chang YQ, Zhang YW. Microstructure and mechanical properties of oxide dispersion strengthened FeCoNi concentrated solid solution alloys. J Alloys Compd. 2020;820:153104.
[30] Jagetia A, Nartu M, Dasari S, Sharma A, Gwalani B, Banerjee R. Ordering-mediated local nano-clustering results in unusually large Hall-Petch strengthening coefficients in high entropy alloys. Mater Res Lett. 2021;9(5):213.
[31] Dasari S, Jagetia A, Sharma A, Nartu M, Soni V, Gwalani B, Gorsse S, Banerjee R. Tuning the degree of chemical ordering in the solid solution of a complex concentrated alloy and its impact on mechanical properties. Acta Mater. 2021;212:116938.
[32] Wu Z, Bei H, Pharr GM, George EP. Temperature dependence of the mechanical properties of equiatomic solid solution alloys

with face-centered cubic crystal structures. Acta Mater. 2014;81:428.
[33] An XL, Zhao H, Dai T, Yu HG, Huang ZH, Guo C, Chu PK, Chu CL. Effects of heat treatment on the microstructure and properties of cold-forged CoNiFe medium entropy alloy. Intermetallics. 2019;110:106477.
[34] Yang MX, Pan Y, Yuan FP, Zhu YT, Wu XL. Back stress strengthening and strain hardening in gradient structure. Mater Res Lett. 2016;4(3):145.